PASSIVE SUPERCONDUCTING FLUX CONSERVERS FOR ROTATING-MAGNETIC-FIELD–DRIVEN FIELD-REVERSED CONFIGURATIONS

C. E. MYERS,* M. R. EDWARDS, B. BERLINGER, A. BROOKS, and S. A. COHEN

Princeton Plasma Physics Laboratory, Princeton, New Jersey 08543

The Princeton Field-Reversed Configuration (PFRC) experiment employs an odd-parity rotating-magnetic-field (RMF_o) current drive and plasma heating system to form and sustain high-β plasmas. For radial confinement, an array of coaxial, internal, passive flux conserver (FC) rings applies magnetic pressure to the plasma while still allowing radio-frequency RMF_o from external coils to reach the plasma. The 3-ms pulse duration of the present experiment is limited by the skin time τ_{fc} of its room-temperature copper FC rings. To explore plasma phenomena with longer characteristic times, the pulse duration of the next-generation PFRC-2 device will exceed 100 ms, necessitating FC rings with $\tau_{fc} > 300$ ms. In this paper we review the physics of internal, discrete, passive FCs and describe the evolution of the PFRC's FC array. We then detail new experiments that have produced higher-performance FC rings that contain embedded high-temperature superconducting (HTS) tapes. Several HTS tape winding configurations have been studied, and a wide range of extended skin times, from 0.4 s to >10³ s, has been achieved. The new FC rings must carry up to 2.5 kA of current to balance the expected PFRC-2 plasma pressure, so the dependence of the HTS-FC critical current on the winding configuration and operating temperature has also been studied. From these experiments, the key HTS-FC design considerations have been identified and HTS-FC rings with the desired performance characteristics have been produced.

KEYWORDS: *field-reversed configuration, rotating magnetic field, flux conserver*

Note: Some figures in this paper are in color only in the electronic version.

I. INTRODUCTION

A steady-state field-reversed configuration (FRC) fusion reactor, e.g., see Momota et al.,[1] would have many attractive features including inherently high-β operation ($\beta \equiv$ plasma pressure/magnetic-field energy density) and relative simplicity of construction. To produce a practical steady-state FRC reactor, however, systems must be developed to stabilize, heat, and sustain FRC plasmas. One of the leading candidates for FRC sustainment[2] and heating[3] is the rotating-magnetic-field (RMF) method. Here, a coil array—also called an antenna set—is used to rotate a perturbative magnetic field through the plasma. The RMF coil array, which is usually external to the FRC's electrically nonconducting vacuum vessel, operates at a radio frequency (rf) near the ion-cyclotron range of fre-

quencies. Because of several theoretically predicted unique benefits,[3,4] the RMF mode studied in the Princeton FRC (PFRC) device[5,6] has odd-parity symmetry (RMF_o) (Ref. 7).

For an FRC plasma to achieve equilibrium, a magnetic-flux-conserving external boundary must be enforced. This is most often realized by surrounding the plasma with a quasi-cylindrical current-carrying shell called a flux conserver (FC). The currents carried in the FC apply predominantly radial magnetic pressure to the plasma in order to counter both the thermal pressure of the heated FRC and the outward hoop force from its azimuthal plasma current. (Note that the FRC is described in cylindrical coordinates $\{z, r, \phi\}$, where ϕ is the azimuthal coordinate.) The ends of the FC are left open to permit a natural divertor geometry for the FRC. Thus, the axially directed forces from the plasma pressure are countered by other forces that include (a) magnetic field-line

tension, (b) a midplane-directed pull from the azimuthal plasma current, and (c) magnetic pressure from mirror fields applied beyond each X point of the FRC. The net result is a balanced plasma equilibrium.[8]

The equilibrium-sustaining currents that are carried in the FC can be either actively driven by an external power supply or passively induced by the changing magnetic fields of the FRC plasma itself. Passively driven FCs do not require high-current pulsed power supplies or complex feeder cables that penetrate the vacuum vessel; these technical simplifications may outweigh the more extensive control that is possible with active FCs. Additionally, because FRC formation excludes magnetic flux from inside the FRC's magnetic separatrix and compresses the excluded field against the FC, the use of a passively driven FC allows for a lower initial bias field magnitude B_0 than the central field magnitude ultimately attained in the FRC, $B_e \equiv -B_z(0,0) = B_z(0, r_s)$. For a cylindrical FC, this ratio, called the field amplification factor F_A, is given by

$$F_A = \frac{B_e}{B_0} = \frac{1}{1 - x_s^2} \quad, \tag{1}$$

where

$x_s = r_s/r_{fc}$

r_s = separatrix radius

r_{fc} = FC inner radius.

Because of these technical and physical considerations, we have chosen to use a passively driven FC in the PFRC device.

Because the PFRC's RMF_o antenna set is located outside of its passive FC, the FC must allow the generated RMF_o to penetrate to the plasma. Thus, the PFRC's FC is broken into several (≥ 6) discrete conducting rings. These rings work together to confine the plasma while permitting the RMF_o to pass through the gaps between them. The bulk current carried in each FC ring is induced by the spin-up of the FRC's azimuthal plasma current. Smaller, rapidly oscillating currents on the surface of the FC rings that are induced at the RMF_o frequency will be discussed in Sec. II. The bulk FC currents are governed by the familiar first-order differential equation for an L-R circuit:

$$V_{fc} = -M_{pl,fc} \frac{dI_{pl}}{dt} = R_{fc} I_{fc} + L_{fc} \frac{dI_{fc}}{dt} \quad, \tag{2}$$

where

V_{fc} = azimuthal loop voltage around the FC

I_{fc} = induced current carried by the FC

L_{fc} = FC self-inductance

R_{fc} = FC resistance

$M_{pl,fc}$ = mutual inductance between the plasma and the FC

I_{pl} = plasma current.

Dividing through by L_{fc} gives

$$-\left(\frac{M_{pl,fc}}{L_{fc}}\right)\frac{dI_{pl}}{dt} = \left(\frac{1}{\tau_{fc}}\right)I_{fc} + \frac{dI_{fc}}{dt} \quad, \tag{3}$$

where the constant $\tau_{fc} \equiv L_{fc}/R_{fc}$ is the e-folding skin time of the FC.

Presently, the PFRC's FC rings are made from oxygen-free, high-conductivity (OFHC) copper. At room temperature these FC rings have $\tau_{fc} \simeq 3$ ms, a seemingly adequate value for plasmas with an energy confinement time τ_E of $<5~\mu$s and a similarly short classical plasma skin time τ_{pl}. However, the phenomena of RMF_o penetration, density equilibration, and gas flow are much longer, often exceeding 1 ms. Thus, the 3-ms skin time of the existing FC rings is already marginal[5] (see Sec. III for further discussion). To study longer-lived, better-confined plasmas in the larger-radius, higher-field PFRC-2 device now under construction, τ_{fc} must be significantly extended. The experiments described herein lay the foundation for the next-generation, extended-skin-time PFRC FC. In particular, we show that high-temperature superconducting (HTS) materials can be embedded in copper FC rings that are cooled by liquid nitrogen (LN_2) to produce an FC for the PFRC-2 device that has a significantly extended skin time ($\tau_{fc} > 300$ ms).

In Sec. II, we describe the previous and present PFRC FC arrays and the unique set of physics constraints that led to their designs. Then in Sec. III, we describe the target plasma parameters for the upgraded PFRC-2 device and how these parameters impact the required performance of its FC array. Section IV details the design and construction of prototype HTS-FCs; a series of proof-of-principle experiments with these prototypes is presented in Secs. V and VI.

II. THE PFRC FLUX CONSERVER

The FC that is used in the PFRC experiment is designed to be passive and internal to the vacuum vessel, which allows it to conform closely to the plasma edge so as to reduce detrimental plasma contact with the vessel wall. Locating the FC between the four-element, 28-cm-long RMF_o antenna set and the plasma, however, creates constraints on the FC design. If the FC were a solid conducting shell, induced surface currents would strongly reduce the RMF_o strength in the plasma region. To prevent this, the PFRC's FC is instead constructed from an array of discrete, coaxial, passive conducting rings (Fig. 1). The radial extent of an FC ring R_{IO} (to be distinguished from its axial thickness) is i.d./2 $< R_{IO} <$ o.d./2, where
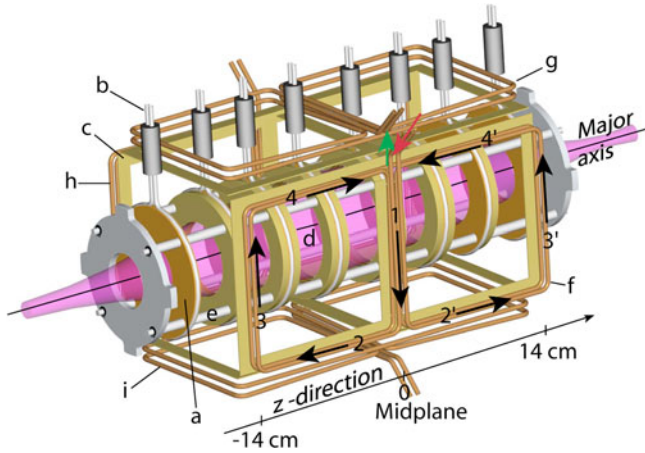
Fig. 1. Sketch of an RMF_o FRC device with internal, discrete FCs: (a) one of eight FC rings, (b) tubing for LN_2 to cool the FC rings, (c) one of four Faraday shields that separate the four antenna elements from the plasma, (d) the plasma, and (e) one of four alumina tubes supporting the eight FC rings. There are four RMF_o antenna elements: one in front (f), one above (g), one behind (h), and one below (i) the plasma. Each element has a figure-eight shape made of seven numbered segments. The black arrows show the direction of the current in antenna element "f" at a particular instant of time. A cylindrical vacuum vessel (not shown here) is located between the Faraday shields and the FCs.

i.d. and o.d. are the FC's inner diameter and outer diameter, respectively.

Each of the four RMF_o antenna elements is composed of seven segments, four parallel (even numbered) and three perpendicular (odd numbered) to the FRC's major axis. The time-varying B_r and B_ϕ fields that are produced by the even-numbered antenna segments are able to expand and contract unimpeded between the rings, but the time-varying B_z field that is generated by the odd-numbered antenna segments must cut through the FC. Thus, the rapidly varying currents induced on the surface of the FC rings will reduce the strength of the RMF_o B_z inside the FC array. To minimize this shielding effect, wide gaps between FC rings are insinuated near the locations of the odd-numbered antenna segments, particularly at $z = 0$ and $z = \pm 14$ cm (see Fig. 1).

To set the stage for formation of high-β plasma discharges in the PFRC, hydrogen gas at 1 mTorr pressure is introduced into the vacuum vessel, and a steady mirror magnetic field is created by external ring coils. (The steady mirror field is left on for hours, so it readily penetrates the FC array.) A low-density seed plasma is formed by a low power (~ 10 W) remote coaxial rf source. High RMF_o power, 5 to 20 kW, is then applied for typically 1 to 10 ms with a repetition rate of 0.5 to 5 Hz. During the first few microseconds, the RMF_o system heats the seed plasma, which increases the ionization rate of the hydro-

gen prefill gas. The plasma density rises to 0.5×10^{12} to 5×10^{12} cm^{-3} while the electron temperature T_e reaches 50 to 400 eV (Ref. 5). The ions remain cold with $T_i \simeq 0.5$ eV. The plasma current builds up as a consequence of electron diamagnetism and electron azimuthal circulation.[9] The plasma duration—more properly, the length of time during which RMF_o power is applied—is chosen to match certain characteristic times of the system. For example, a recent experimental campaign studied effects of neutral hydrogen density on RMF_o penetration and X-ray emission. For these experiments, pulse lengths of 3 ms were adequate to allow control of the neutral density.

On a millisecond timescale, the initial microsecond-duration current spin-up process appears to the FC array as a steplike change in magnetic flux. The induced current response in the FC array from such a steplike driving pulse is given by the Green's function solution to Eq. (2), which takes the form

$$I_{fc}(t) \propto e^{-t/\tau_{fc}} , \qquad (4)$$

such that the time constant τ_{fc} characterizes the duration of induced currents in the FC array. In the experiment, the RMF_o power and frequency may be changed in just a few microseconds during the discharge. Effects associated with these changes are not considered in this paper.

II.A. Analysis of FC Design Considerations

In all theoretical analyses to date of even-parity RMF, e.g., Milroy,[10] the B_z field component, which is produced only near the X points, is considered to be unimportant for driving current or for heating the plasma. Thus, concern for gaps in the FC boundary is minimal. With RMF_o, on the other hand, the B_z field component is strongest near $z = 0$, where it generates a strong azimuthal electric field $\mathcal{E}_\phi \propto \partial B_z / \partial t$ that drives particle heating and current near the O point null line. In order to take advantage of this midplane $\mathcal{E}_\phi$ from the RMF_o system, it is important to understand and mitigate the screening of the time-varying B_z field.

To study the B_z screening effect more quantitatively, it is useful to examine how the B_z screening depends on the size of the gap between adjacent FC rings. This is done here with a series of finite-element simulations from the SPARK code.[11] In each simulation, the RMF_o B_z field is produced by two antenna segments corresponding to the segments "1" of antenna elements "f" and "h" in Fig. 1. These two segments, which carry equal currents in the same direction, are each 14 cm long and located 7 cm from the major axis on opposite sides of the device. The FC rings used in the simulations are $\frac{3}{8}$ in. thick with i.d. = 8.25 cm and o.d. = 10 cm. They are assumed to be perfectly conducting, which is a good approximation for copper on the timescale of the RMF_o field oscillations.

In the first set of simulations, an FC array with four equally spaced FC rings is studied (see Fig. 2a). In particular, the spacing between adjacent rings is varied
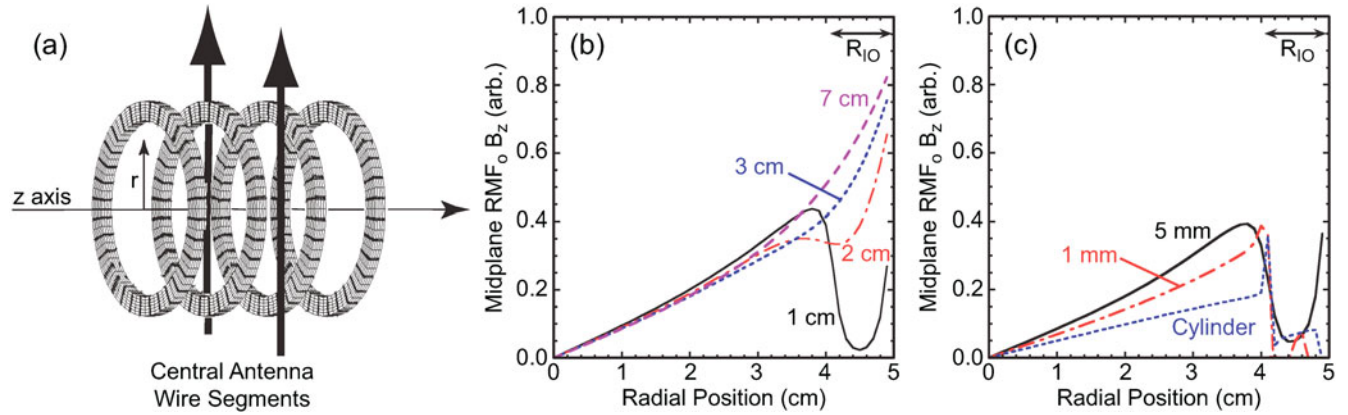
Fig. 2. Effects of the gap width between FC rings on the RMF_o midplane B_z field. (a) Geometry of the simulation. (b) B_z versus r, created by the segments "1" of the "f" and "h" antenna elements, is shown for gaps of 1, 2, 3, and 7 cm. (c) Simulations for a fixed FC array length, 9 cm, and smaller gap sizes.

between 1 and 10 cm. Several of the resulting radial profiles of the RMF_o B_z field at the midplane are shown in Fig. 2b. For gap widths of ≥ 7 cm, the $B_z(r)$ profile varies by $<1\%$ from the case with no FCs at all. For gap widths of ≤ 2 cm, the primary change in $B_z(r)$ occurs in the R_{IO} region. The profile is able to remain relatively consistent for $r <$ i.d./2 because the surface currents on the FC rings move in opposite azimuthal directions on the inner and outer edges of the FC. Thus, these currents mostly cancel each other's effects outside of the R_{IO} region. It is clear, then, that the FC rings can reduce the induced $\mathcal{E}_\phi$, especially near the edges of the FC rings. This assertion is supported by photographs and movies of PFRC plasmas, which show reduced photon emission (and, by extension, plasma density) in the R_{IO} region. Lack of plasma in the R_{IO} region may, however, be an operational benefit because of the reduced plasma-material interactions at the FC surfaces.

A second set of SPARK simulations is used to study the effect of even smaller gaps between the FC rings. The FC array used here has a fixed axial length of 9 cm. Now the number of $\frac{3}{8}$-in. rings in the FC array is determined by the spacing between the rings, which is varied from 0 to 10 mm (see Fig. 2c). Significant reduction of the B_z in the region 0 cm $< r <$ 4 cm is only seen for gap spacings of ≤ 5 mm. Even with a continuous cylinder, 40% of the B_z is able to enter through the cylinder's open ends. Thus, we conclude that as long as the gap spacing at the midplane is a few centimeters wide, the shielding of the RMF_o B_z field remains at an acceptable level.

The segmented nature of the PFRC FC array also significantly affects the shape of the boundary of the FRC plasma. The FIELDCOILS code, which was developed specifically for this project, was used to explore the effects of the discrete FC array on the FRC plasma shape. FIELDCOILS is a Biot-Savart magnetostatics code written with a PYTHON front end and a C++ back end. It

provides customized induced current and magnetic field line calculations for the PFRC device. In these simulations, external coaxial magnetic coils, which correspond to those used in the PFRC experiment,[5] provide a vacuum bias field with a central value of $B_0 = B_z(0,0) =$ 400 G and a maximum mirror field of ~5 kG at $z = \pm 45$ cm. A uniform electron density of $n_e = 1.9 \times 10^{13}$ cm^{-3} is specified inside an elliptical plasma boundary (see Fig. 3). The electrons are assumed to be driven to rotate around the device by the RMF_o fields. In particular, a rigid-rotor electron rotation profile is assumed to exist inside the plasma boundary with $\omega_{RR} = \omega_{RMF} = 2.5 \times 10^7$ rad/s. The rotating electrons generate the azimuthal plasma current I_{pl} and hence a dipole like magnetic field. The eight FC rings shown in Fig. 3 have the dimensions of the rings that are presently being constructed for the PFRC-2 device.

The net field from the rotating electrons, the external magnets, and the induced currents in the FCs creates the corrugated flux surfaces—actually field lines—that are shown in Fig. 3. A separatrix forms with $r_s \simeq 6.5$ cm at
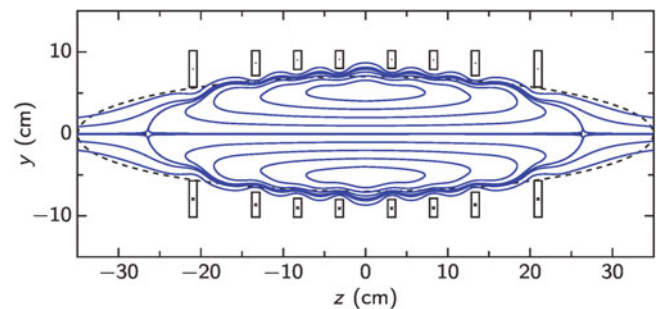

Fig. 3. Flux surfaces of an elliptic rigid-rotor current profile inside an array of eight coaxial FCs. The dashed line shows the extent of the current-carrying region.
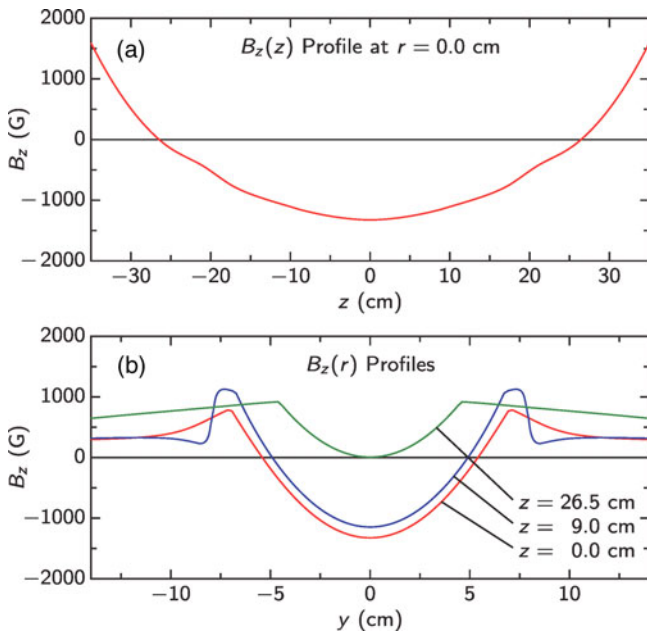
Fig. 4. (a) Axial and (b) radial profiles of B_z for the system shown in Fig. 3. Field reversal is evident from the negative values of B_z in the plasma region. The radial profile at $z = 9.0$ cm shows the deformation of the field near one of the FC rings.

$z = 0$. The X points lie well inside the current-carrying region, while the separatrix lies outside the ellipse at the midplane. Plasma stability against the tilt mode could be improved by the corrugated flux surfaces and the finite plasma pressure and current outside the separatrix. Self-consistent studies of these effects with fully kinetic codes are only now beginning.[9] Radial and axial line-outs of B_z (Fig. 4) show that the central magnetic field is increased from the initial value of 400 G to 1200 G, which corresponds to a field amplification factor of $F_A \simeq 3$.

II.B. Evolution of the PFRC FC Array Design

Within the design constraints discussed above, the FC array that is used in the PFRC experiment has undergone three generations of development prior to the present push to incorporate HTS materials. The first array consisted of 14 copper rings, the second 10, and the third 6. Concurrently, the i.d. of each FC ring was increased from 5 to 7 to 8.25 cm (for the rings nearest the midplane), and each ring's thickness increased from $\frac{1}{8}$ to $\frac{1}{4}$ to $\frac{3}{8}$ in. Motivating these changes was the need to achieve better radial plasma confinement and better penetration of the RMF_o B_z field through the FC array.

The FC rings are located inside the main vacuum vessel and are therefore the primary plasma-facing component. The remote divertor plates intersect open field lines about 1 m from the midplane. In the presently op-

erating PFRC-1 device, they experience a heat load of nearly 5 MW/m². As plasma performance improved markedly with better RMF_o antennae, FC designs, and operational technique, copper from the surface of the rings began to sputter and coat the Pyrex vacuum vessel walls. To alleviate this problem in the third generation of the PFRC-1 device, 0.005-in.-thick tantalum foil shields were placed on the plasma-facing surfaces of the copper FC rings. Figure 5 shows the present tantalum-shielded FC array.

The tantalum shields were first treated in a separate vacuum vessel with a neon glow discharge to burn away asperities prone to arcing. Subsequently (in the PFRC vacuum vessel) a nitrogen glow discharge was applied with the intention of forming a diffusion barrier on the tantalum to reduce its ability to absorb hydrogen from (or release it into) the FRC plasma. This latter step was performed to counter unwanted increases in plasma density observed on the first day of operations with the Ta-covered FCs. Since the installation of the tantalum shields, over 700 000 discharges have been logged, corresponding to about 2×10^3 seconds of plasma and an estimated hydrogen fluence to the Ta shields of 2×10^{21} cm⁻². The best n_e and T_e achieved were slightly higher than the best achieved without the Ta. The maximum excluded magnetic flux, Φ_{ex}, was about 150% higher. All improvements are attributed to increases in r_{fc}, r_s, and B_0, made possible by increased RMF_o power and wider FC gaps. No sputtering issues, such as increased radiative losses or coatings on the Pyrex vacuum vessel, have arisen. No degradation of the shields, such as cracking due to hydrogen embrittlement, is yet evident. Based on this prior experience, the FC rings in the PFRC-2 device will be
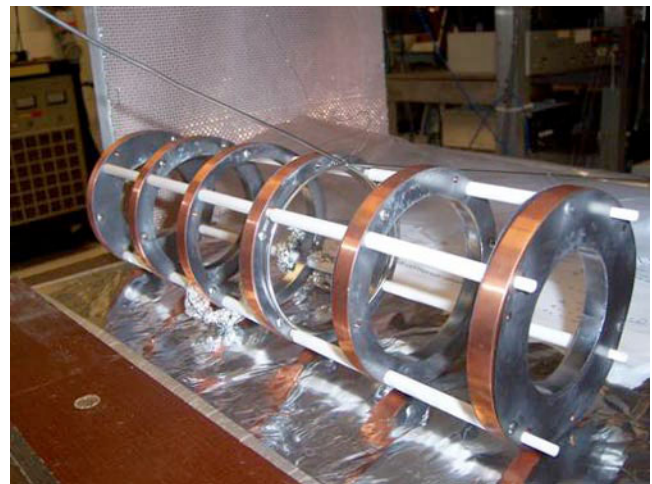

Fig. 5. The present FC array, which has six coaxial $\frac{3}{8}$-in.-thick OFHC copper FCs, each covered, on plasma-exposed surfaces, by 0.005-in.-thick tantalum foil to reduce sputtering. Insulating alumina rods (white) provide structural support to the array.

similarly shielded. In this iteration, however, boron nitride was chosen over tantalum, primarily for its lower-Z composition.

III. TARGET PLASMA AND HTS-FC PARAMETERS FOR THE PFRC-2 DEVICE

Despite having energy confinement times τ_E and particle confinement times τ_p in the microsecond range, many phenomena observed in the PFRC experiment have characteristic times that exceed 1 ms. One example is RMF_o penetration. When each plasma discharge is initiated, the best coupling is obtained with the resonant frequency of the rf system shifted slightly above the vacuum resonance frequency. The amount of the shift is consistent with a reduced system inductance that results when the RMF_o fields are excluded from the interior of the plasma column.[5] As the plasma evolves, its parameters, such as n_e and Φ_{ex}, change (Fig. 6a). In response, the rf coupling begins to decline at $t \simeq 1$ ms (Fig. 6b). To compensate for the change in rf coupling, the RMF_o frequency is lowered
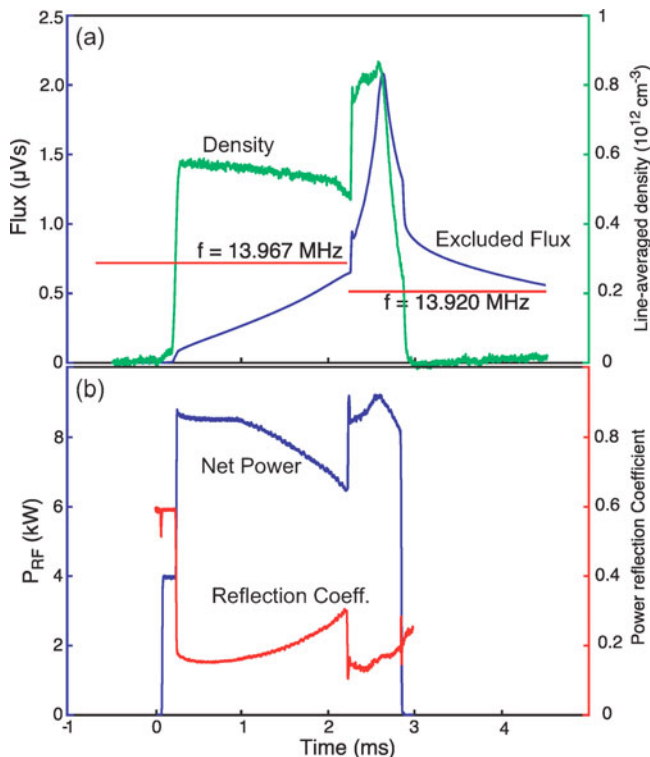

Fig. 6. (a) Typical density and excluded flux traces from the PFRC. The density begins to fall at a faster rate at $t \simeq 2$ ms. At $t = 2.2$ ms, the RMF_o frequency is shifted from 13.967 to 13.920 MHz, which markedly increases both n_e and Φ_{ex}. (b) The change in RMF_o frequency also improves the power coupling between the RMF_o system and the plasma.

to the vacuum resonance value—an action labeled "frequency modulation"—at $t = 2.2$ ms. At this time, n_e and Φ_{ex} rapidly rise as good rf coupling is restored. The growth in n_e and Φ_{ex} in response to the RMF_o frequency shift to the vacuum resonance frequency is a strong indication that the RMF_o has now penetrated to the axis of the plasma column. Unfortunately, by $t \simeq 3$ ms the currents in the room-temperature OFHC copper FC array have decayed to ~40% of their initial value.

Additional long-timescale effects in the PFRC device include density control and impurity control. Density control in the PFRC-1 device has a characteristic time that is ~100 times longer than τ_E due to both the slow emptying of gas lines attached to the vacuum vessel and plasma recycling effects. With regard to recycling, the effective particle confinement time τ_p^* is given by $\tau_p^* \sim \tau_p/(1-R)$, where R is the recycling coefficient.[12] In the PFRC device, R is close to unity such that $\tau_p^* \gg \tau_p$. Based on our spectroscopic observations of impurities, impurity control requires similarly lengthy timescales because of both ionization rates and confinement. This situation may be exacerbated in the PFRC-2 device as the progressively hotter plasma bombards the boron nitride shields and releases more deeply adsorbed gases and sputtering impurities. Upgrading the PFRC facility to facilitate longer pulses will thus allow detailed studies of longer-timescale plasma behavior, including RMF_o resonances, low-frequency plasma fluctuations, and fueling/recycling processes.

Though accessing the quasi-steady-state, RMF_o-penetrated regime is an important motivation for pursuing high-performance superconducting FC rings, the primary reason is to allow studies of RMF_o/FRC plasmas with longer energy confinement times τ_E. If τ_E is classical, it is expected to increase $\propto r_s^2 B_e^2 T_e^{3/2}$. The goal of the PFRC-2 device is to reach parameters of $B_e = 1.3$ kG, $n_e = 10^{13}$ cm^{-3}, $T_i = 1.5$ keV, and $T_e = 1$ keV. If the energy losses were five times faster than the classical rate, τ_E would exceed 10 ms, which is much longer than required to sustain kilo-electron-volt-temperature plasmas with the available RMF_o power. Discharges in the PFRC-2 that are sustained for $\sim 10\tau_E \simeq 100$ ms can be considered steady state. To ensure that the currents induced in the FC rings will persist throughout the discharge, τ_{fc} must be about three times longer than the planned maximum discharge duration. To extend τ_{fc}, the ratio of the FC inductance to resistance must be increased by about a factor of 100. Since the inductance is relatively fixed, reducing the resistance by a large factor requires the use of superconducting materials. To ease implementation, HTS tapes are used.

There is also, however, an upper limit to the useful τ_{fc} in the PFRC-2 device. It is desirable that the FC current decay quickly enough that the applied B_0 can be readily changed to accommodate scans of experimental parameters. Based on this criterion and a 1% duty factor that is set by the rf power supply system, the maximum

Target HTS-FC Parameters

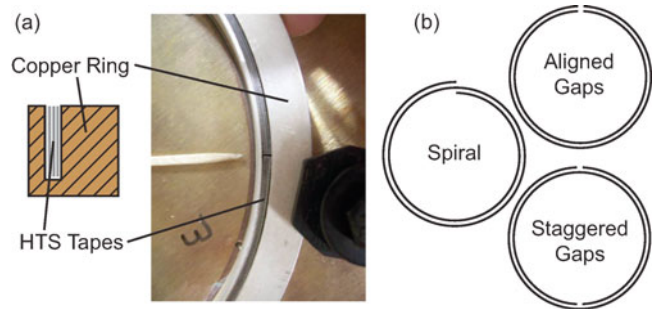|	τ_{fc} (min)	τ_{fc} (max)	I_{cr}
OFHC Cu-FC (295 K)	3.2ms	—	—
OFHC Cu-FC (77 K)	28.0ms	—	—
HTS-FC (77 K)	0.3 s	3.0 s	2.5 kA

Fig. 7. (a) Top and cross-sectional views of the modified FC ring with HTS tapes embedded in the trench, which has not yet been filled with solder. This Cu ring has been plated with Ni/Ag. A toothpick points to the aligned gaps. (b) Possible winding configurations for HTS-FC rings with 2 turns of HTS tape. The different configurations produce markedly different skin times and critical currents.

desirable τ_{fc} for the HTS-FC rings is ~3 s for 100-ms plasma pulses.

One complication that is introduced when superconducting materials are included in the FC design is that the material becomes resistive when the magnetic field at its surface exceeds a temperature-dependent critical value. Often it is the self-field produced by currents in the superconductor that exceeds this magnetic field threshold. This leads to the concept of critical current I_{cr}, a property of the superconductor, its temperature, and the field strength and geometry, i.e., whether the external fields are normal to or parallel to the superconductor surface. If this critical current is exceeded, the superconductor becomes resistive and no longer provides extended-skin-time FC performance.

Because of the large FRC plasma currents and the correspondingly large induced currents in the FC rings, there must be enough HTS material in each FC to carry the heavy current load without exceeding I_{cr}. Magnetostatic induced current calculations from the FIELD-COILS code indicate that the peak current load for the FC rings will be near 2.5 kA. The target FC parameters discussed in this section are summarized in Table I.

IV. HTS-FC DESIGN AND CONSTRUCTION

Advances in HTS technology have led to commercially available products that are practical and affordable for use in the PFRC experiment. The HTS product chosen for this project is the first-generation, BSCCO-based, high-current-density wire.[a] This wire comes as a 4.4-mm-wide, 0.26-mm-thick stainless steel–clad ribbon (tape) with a nominal critical current capacity of $I_{tape} \simeq 160$ A at 77.3 K. Our experiments also include some HTS-FCs that were constructed with an alternate 3-mm-wide tape that has a lower critical current of $I_{tape} \simeq 64.2$ A. The ability to use LN_2 to cool the HTS tapes rather than a harder-to-handle coolant such as liquid helium is central to the viability of this HTS-FC design.

The design paradigm for the HTS-FC rings is shown in Fig. 7a. A prototype 11-cm-i.d. OFHC copper FC ring

---

[a]Produced by American Superconductor Corp., Devens; Massachusetts 01434.

is modified by milling a deep trench near its i.d. wall. Multiple lengths of HTS tape are then placed in this trench, which is then backfilled with solder. The solder provides an electrical and thermal bond between the HTS tape and the surrounding copper. It also mechanically stabilizes the configuration.

The soldering is accomplished by heating the entire FC ring on a hot plate to a well-controlled temperature that is above the melting point of the solder. Because the HTS material's nominal damage threshold of 179°C is lower than the melting point of traditional eutectic 63/37 Sn/Pb solder (183°C), a specialized lower-melting-point solder was originally pursued for this project. In particular, an indium alloy solder (97/3 In/Ag) that melts at 143°C was used to avoid damaging the HTS tapes during soldering. This In/Ag solder, which was recommended by American Superconductor, was successfully used to produce the first few HTS-FC rings.

The use of In/Ag solder introduces complications to the HTS-FC fabrication process. To be compatible with the In/Ag solder, the copper FC ring must be plated first with nickel and then with silver. Even with this modification, the surface chemistry of the In/Ag solder is still somewhat poor, as it is reluctant to wet to the materials in the trench. Later tests showed that, though eutectic Sn/Pb solder melts above the damage threshold for the HTS tapes, it could be used to produce HTS-FC rings with the same performance characteristics as those produced with In/Ag solder. To accomplish this, the tapes must be held securely in the trench during heating so that they do not deform when the damage threshold is exceeded. Unlike the In/Ag solder, the Sn/Pb solder has excellent surface chemistry with the copper and the factory pretreated stainless steel cladding of the HTS tapes. Because the In/Ag solder is significantly more expensive than Sn/Pb solder, using the latter product also serves to reduce the cost of the HTS-FC manufacturing process.

As discussed in Sec. III, the PFRC-2 device will require specific performance parameters from its HTS-FC rings (see Table I). To meet the required 2.5-kA critical current capacity, >20 turns of HTS tape must be used in each HTS-FC ring due to the $I_{tape} \simeq 160$ A limitation of each tape. As shown in Fig. 7b, there are three primary ways to wind multiple turns of HTS tape in the FC ring (aligned gap, staggered gap, and spiral). Each winding configuration results in different performance characteristics from the finished HTS-FC ring. Without empirically testing each of these configurations, it is unclear how they will influence the attainable τ_{fc} and I_{cr} values.

V. HTS-FC TESTING AND ANALYSIS

The experimental performance of a single FC ring may be quantified by imposing a strongly changing magnetic flux in the cross section of the ring. This serves to emulate the spin-up of the FRC plasma current. The resulting currents that are induced in the FC ring can be measured to characterize its performance. To this end, a stand-alone HTS-FC test facility was constructed to quantify the performance of candidate FC rings in a controlled environment.

V.A. The Experimental Facility

A diagram of the facility that was designed and constructed to test candidate FC rings is shown in Fig. 8. A high-current driving circuit is connected across the windings of the primary solenoid to provide the desired magnetic flux swing in the center of the FC ring. The candidate ring is placed in a thermally isolated section of the device that is near the top of the solenoid. Here, the ring can be submerged in an LN_2 bath and cooled to 77.3 K. To diagnose the behavior of the system, the time-resolved magnetic field signal is collected by an F. W. Bell Series 5180 Hall-effect Gaussmeter that is placed on the axis of the system. This Hall probe measures the axially directed component of the magnetic field (B_z) at its tip. Room-temperature air is forced up through the hollow center stack of the device to maintain the Hall probe at room temperature in order to ensure the stability and accuracy of its measurements.

As shown by the field lines in the right half of Fig. 8, the current induced in the FC ring prevents the magnetic field that is produced by the primary windings from penetrating fully to the axis of the device. Thus, the Hall probe will measure a reduced signal when the FC ring is in the system. If the primary driving waveform $I_{dr}(t)$ is carefully chosen, the skin time of the FC ring τ_{fc} can be extracted from these measurements. Two specific techniques for measuring τ_{fc} (and eventually I_{cr}) are discussed in Secs. V.B and V.C: the "AC phase-delay" technique and the "DC current-decay" technique.
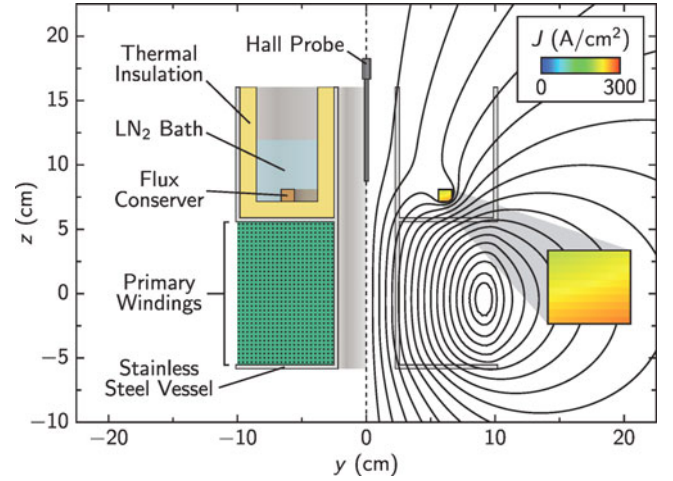

Fig. 8. Schematic of the cylindrically symmetric HTS-FC test facility. Magnetic flux is driven through the FC by the primary windings. The resulting axial magnetic field profile is measured by the Hall probe on the axis of the device. The field lines in the right half of the figure show that the currents induced in the FC cross section prevent the magnetic field from fully penetrating to the axis. The square inset (to the right) is an enlargement of the FC cross section that shows the current density distribution within the FC ring. In this case, the FC ring is solid copper at room temperature and is driven by a sinusoidal current in the primary windings with a frequency of $f = 60$ Hz.

V.B. The AC Phase-Delay Technique

One measurement technique that is useful for characterizing short skin-time rings ($\tau_{fc} < 50$ ms) is the AC phase-delay technique. Here, the circuit is driven with a sinusoidal function:

$$I_{dr}(t) = I_{dr,0} \cos(\omega t) \ , \qquad (5)$$

where ω is the driving frequency and the "0" subscript on $I_{dr,0}$ denotes the constant signal amplitude. The resulting solution to the L-R circuit ordinary differential equation [Eq. (3)] with $I_{dr}(t)$ replacing $I_{pl}(t)$ is a phase-delayed sinusoid of the form

$$I_{fc}(t) = -I_{fc,0} \cos(\omega t - \phi) \ , \qquad (6)$$

where the overall negative sign results from the application of Lenz's law. The amplitude $I_{fc,0}$ is a function of the driving amplitude $I_{dr,0}$, the inductance ratio $M_{dr,fc}/L_{fc}$, and the dimensionless timescale $\omega \tau_{fc}$; the phase delay ϕ is given by

$$\phi = -\tan^{-1} \left(\frac{1}{\omega \tau_{fc}} \right) \ . \qquad (7)$$

Thus, if the phase delay ϕ and the driving frequency ω can be measured experimentally, the skin time τ_{fc} can be calculated from these measurements.

A bipolar amplifier is used to provide the high-current sinusoidal driving waveform [Eq. (5)] at frequencies ranging from 10 to 500 Hz. The current flowing in the primary solenoid is directly measured using a Pearson Model 110A current transformer. On the time and length scales of interest, the system is magnetostatic, which implies that the magnetic field signals measured by the Hall probe are directly proportional to the currents that generated them. Thus, the phase delay ϕ can be extracted directly from measurements of the magnetic field.

Measuring ϕ experimentally is a multistep procedure that requires comparing Hall probe signals that are obtained with and without the candidate FC ring present in the system. With the FC ring in the system, the Hall probe measures a time-varying axial magnetic field $B_m(t)$ that is a superposition of the field produced by the primary solenoid $B_{dr}(t)$ and the field produced by the ring $B_{fc}(t)$. Without the FC ring in the system, the measured value of B_m is simply equal to B_{dr} at the probe's location. Defining α to be the phase delay in the measurement of B_m, the various signals can be written as

$$B_{dr}(t) = B_{dr,0}\cos(\omega t) \ ,$$

$$B_{fc}(t) = -B_{fc,0}\cos(\omega t - \phi) \ ,$$

and

$$B_m(t) = B_{m,0}\cos(\omega t - \alpha) = B_{dr}(t) + B_{fc}(t) \ . \quad (8)$$

By combining Eqs. (8) and zeroing the time dependence in each term, ϕ and $B_{fc,0}$ are found to be

$$\tan\phi = -\frac{B_{m,0}\sin\alpha}{B_{dr,0} - B_{m,0}\cos\alpha} \quad (9)$$

and

$$B_{fc,0} = -\frac{\sin\alpha}{\sin\phi}B_{m,0} \ . \quad (10)$$

Here, $B_{dr,0}$ is obtained from the signal acquired without the ring in the system, while both $B_{m,0}$ and α are obtained from the signal acquired with the ring. Thus, the phase delay ϕ and hence the skin time τ_{fc} can be determined using Eq. (9).

Two corrective subtleties were discovered during the experimentation process. The first is a correction to the measured values of α. Without the FC ring in the system, a nonzero phase shift $\alpha_{dr} \simeq 9°$ was consistently observed between the $B_{dr}(t)$ signal measured by the Hall probe and the $I_{dr}(t)$ signal measured by the Pearson current transformer. In free space, no phase shift is expected in this configuration. Simulations of currents induced in the

stainless steel winding form indicate that these currents produce ~60% of the observed α_{dr} phase shift. The remaining 40% of the measured shift is consistent with the bandwidth of the Hall probe and Pearson electronics. Assuming that the same background shift α_{dr} is present with and without the FC ring, Eqs. (9) and (10) are corrected by making the substitution $\alpha \to \alpha - \alpha_{dr}$.

The second corrective subtlety is that the measured $B_{dr,0}$ amplitude is underestimated because slightly different currents flow in the primary solenoid with and without the FC ring in the system. This small change is consistent with a change in the overall system inductance due to the presence or absence of the FC ring. The measurement of $B_{dr,0}$ must be obtained without the FC ring in the system, so the $B_{dr,0}$ value used in Eq. (9) is scaled by the ratio of the driving solenoid currents measured by the Pearson current transformer with and without the FC ring in the system: $B_{dr,0} \to (I_{dr,0}/I'_{dr,0})B_{dr,0}$, where $I_{dr,0}$ is the primary current flowing with the FC ring and $I'_{dr,0}$ is the primary current without the ring. These corrections to the measured values of both α and $B_{dr,0}$ are central to the accurate characterization of the FC rings.

Figure 9 shows data obtained using the AC phase-delay technique for various probe locations along the z-axis of the device. These measurements are compared to numerical calculations of the expected values for these
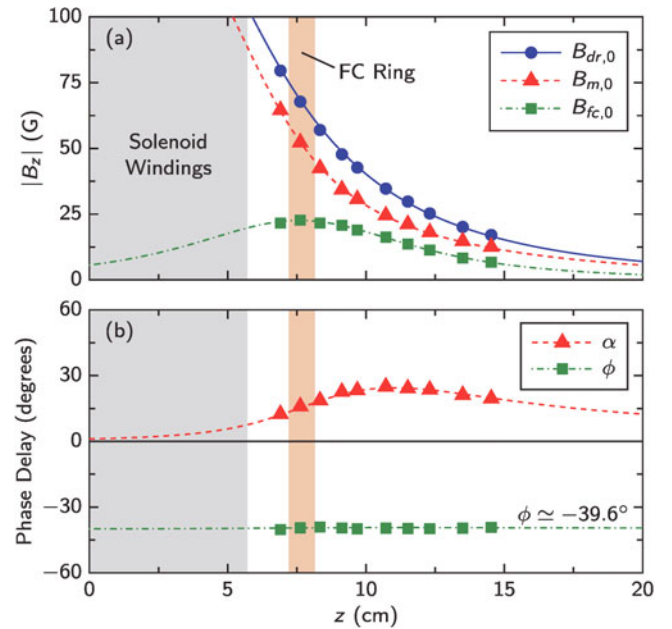

Fig. 9. Comparison of experimentally measured and numerically computed AC phase-delay data spanning a range of axial measurement locations. The plotted experimental values of ϕ and $B_{fc,0}$ were calculated using Eqs. (9) and (10). The numerical curves were computed using the FIELDCOILS code. The agreement between the numerical calculations and the experimental data is excellent.

measurements (as opposed to fitted functions). The numerical curves are computed using the FIELDCOILS magnetics code, which was introduced in Sec. II. The code models the geometry of the primary solenoid and the FC ring as a single system. Here, the resistance of the ring is taken to be that of OFHC copper (17.1 n$\Omega \cdot$m). Its self-inductance is computed numerically such that the skin time can be calculated from these two values. Finally, the mutual inductance between the solenoid and the ring is computed such that the only remaining parameters are the driving frequency ω and the primary current $I_{dr,0}$. The agreement between these calculations and the measurements is excellent, suggesting that the measurements of the skin time τ_{fc} using this technique are quite accurate.

The AC phase-delay technique was used to measure the baseline skin times of both room-temperature and LN$_2$-cooled OFHC copper FC rings. The phase delay measured for the room-temperature copper ring was $\phi \simeq -39.6°$ (see Fig. 9); this corresponds to a skin time of $\tau_{fc} \simeq 3.2$ ms. For the LN$_2$-cooled ring, a phase delay of $\phi \simeq -5.4°$ was measured, which corresponds to a longer skin time of $\tau_{fc} \simeq 28.0$ ms. Since the resistivity of copper changes from 17.1 n$\Omega \cdot$m to 2.1 n$\Omega \cdot$m when cooled with LN$_2$, the measured change in the skin time ($28.0/3.2 \simeq 8.8$) agrees with the expected change in the resistivity ($17.1/2.1 \simeq 8.1$).

The AC phase-delay technique works well for FC rings with 0.5 ms $< \tau_{fc} < 50$ ms at the reasonable driving frequency of $f = 60$ Hz. Outside this range, however, the value of α at $z = 10$ cm drops below a few degrees, thereby introducing unacceptable error into the measurement of τ_{fc}. Consequently, this technique is not adequate for measuring the much longer skin times of the high-performance HTS-FC rings under consideration.

V.C. The DC Current-Decay Technique

For FC rings with skin times longer than those that are suitable for the AC phase-delay technique, a different measurement procedure is needed. As indicated in Eq. (4), if $I_{dr}(t)$ is a step function of the form

$$I_{dr}(t) = I_{dr,0}H(t) \ , \tag{11}$$

where $H(t)$ is the Heaviside step function, then the FC ring will respond with a time-decaying current given by

$$I_{fc}(t) = -I_{dr,0}\left(\frac{M_{dr,fc}}{L_{fc}}\right)e^{-t/\tau_{fc}} \ . \tag{12}$$

Thus, the logarithm of this decaying current will be a line with slope $m = -1/\tau_{fc}$, which presents another way to measure τ_{fc}. This DC current-decay measurement technique can be used to characterize FC rings with much longer skin times than those measured with the AC phase-delay technique.

In practice, it is not possible to impose a step function change in $I_{dr}(t)$ [as in Eq. (11)] due to the finite inductance and resistance of the primary solenoid. Instead, a step function voltage of the form

$$V_{dr}(t) = V_{dr,0}H(t) \tag{13}$$

is applied which, in turn, produces a driving current of the form

$$I_{dr}(t) = I_{dr,0}(1 - e^{-t/\tau_{dr}}) \ , \tag{14}$$

where $\tau_{dr} = L_{dr}/R_{dr}$ is the characteristic rise time of the primary solenoid. The primary solenoid has a sizeable self-inductance ($L_{dr} \simeq 32.8$ mH), so τ_{dr} is not negligible ($\tau_{dr} \simeq 18.5$ ms). Thus, when driven by the $I_{dr}(t)$ waveform in Eq. (14), the induced current in the FC ring will not approach the Green's function form of Eq. (12) until $t \gg \tau_{dr}$. This places a lower bound on the FC skin times that can be measured using this technique. In practice, this method is suitable for measuring FC rings with $\tau_{fc} > 100$ ms. For this reason, the previously discussed AC phase-delay measurement technique was developed for characterizing OFHC copper FC rings, which have much shorter skin times.

The implementation of the DC current-decay measurement technique is similar to the AC phase-delay technique in that Hall probe signals must again be acquired with and without the FC ring present in the system. The signal with the ring present, labeled $B_m(t)$ as before, is subtracted from the signal acquired without the ring, $B_{dr}(t)$, in order to find the magnetic field produced by the FC:

$$|B_{fc}(t)| = B_{dr}(t) - B_m(t) \ . \tag{15}$$

Magnetic signals from a sample DC current-decay measurement are plotted in Fig. 10a. As with the AC phase-delay technique, the signal with the FC ring present, $B_m(t)$, is reduced from the non-FC signal, $B_{dr}(t)$, because the current flowing in the FC ring opposes that of the current in the primary. All signals using the DC current-decay technique are acquired with the probe at $z = 10$ cm, where the field reduction is very strong. The $B_{dr}(t)$ signal is normalized to $B_m(t)$ very late in time ($t_{norm} > 5\tau_{fc}$) to ensure that the difference of the two signals, $|B_{fc}(t)|$, decays to zero. This normalization typically adjusts the amplitude of $B_{dr}(t)$ by $<0.5\%$. Currents in the stainless steel winding form need not be considered as they were with the AC phase-delay method because these currents decay on a timescale that is much faster than the driving current rise time ($\tau_{wf} \simeq 0.16$ ms $\ll \tau_{dr}$).

The magnetostatic approximation once again applies, so B_{dr} and B_{fc} can be related to I_{dr} and I_{fc} with geometric constants of proportionality. These constants were calculated using the FIELDCOILS code for $z = 10$ cm, where the signals were acquired. The logarithm of the resulting current waveform $I_{fc}(t)$ is shown in Fig. 10b. The "expected" $I_{fc}(t)$ waveform is numerically
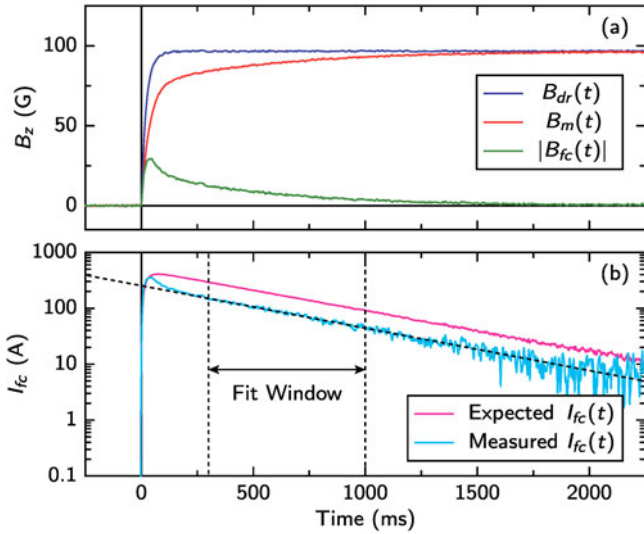
Fig. 10. (a) Hall probe signals acquired for DC current-decay analysis of an HTS-FC ring with 5 turns of 3-mm-wide HTS tape ($I_{tape} \simeq 64.2$ A). The $|B_{fc}(t)|$ signal is the difference between the acquired $B_{dr}(t)$ signal and $B_m(t)$ signal. (b) The measured $I_{fc}(t)$ waveform is scaled magnetostatically from the $|B_{fc}(t)|$ signal, while the "expected" waveform is numerically computed from the measured $B_{dr}(t)$ signal. The difference between the two is a consequence of additional resistive dissipation due to critical current saturation of the HTS material early in time. The skin time of this 11-cm-i.d. aligned-gap HTS-FC ring at 77.3 K is $\tau_{fc} \simeq 570$ ms.
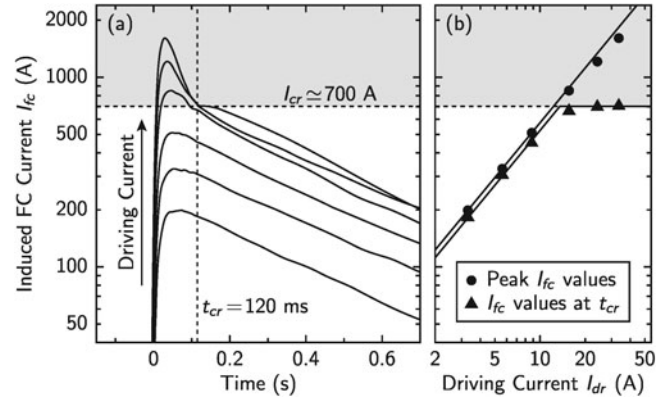

Fig. 11. (a) Demonstration of the onset of critical current effects with increasing driving current. The waveforms transition from those with a single characteristic decay time at weaker driving currents to those with a two-part decay process at stronger driving currents. (b) Transcription of the peak and critical I_{fc} values to more clearly illustrate the critical current saturation. The reason that the FC currents are initially able to exceed the critical current threshold is because shorter-lived currents are carried by the copper that surrounds the HTS tapes. The FC used here is a 5-turn, aligned-gap FC that contains HTS tapes with $I_{tape} \simeq 160$ A.

computed using the measured $B_{dr}(t)$ waveform to supply the driving current $I_{dr}(t)$. The visible difference between the expected and measured waveforms is indicative of critical current saturation of the superconductor early in time. This effect will now be discussed in more detail.

V.D. Critical Current Measurements

The measured $I_{fc}(t)$ waveform in Fig. 10b diverges from the "expected" waveform when the FC current is near its maximum (20 ms < t < 120 ms). During this time, the measured current decays very quickly. After the FC current has fallen a certain amount, however, it abruptly resumes its decay at the "expected" rate. This peculiar behavior is explained by the onset of critical current saturation in the superconductor during the high-current portion of the $I_{fc}(t)$ waveform. Once the superconductor saturates, it becomes highly resistive such that any further induced currents are only carried by the surrounding copper. These supersaturated currents quickly decay with the LN$_2$-cooled-Cu skin time of $\tau_{fc} \simeq 28$ ms. Only when the critical current threshold is recrossed does the HTS-FC ring return to its nonsaturated behavior.

This critical current behavior is examined in more detail in Fig. 11. $I_{fc}(t)$ waveforms are displayed for various driving current amplitudes I_{dr} (Fig. 11a). At the weaker driving currents, the waveform decays with a single characteristic time. At the stronger driving currents, however, the previously described two-part decay process emerges. The onset of this two-part decay process indicates that the critical current threshold of this HTS-FC ring has been exceeded. This behavior can be seen very clearly in Fig. 11b, where the peak I_{fc} value and the I_{fc} value at $t \equiv t_{cr} = 120$ ms are plotted for each waveform in Fig. 11a. It is clear that by the "critical time" t_{cr} the FC current is clamped to a critical current value of $I_{cr} \simeq 700$ A.

Though it is relatively straightforward to pinpoint the critical current value I_{cr} for the HTS-FC examined in Fig. 11, consistently determining I_{cr} for the wide variety of HTS-FCs studied during this project is not a trivial process. In particular, HTS-FCs with much longer skin times ($\tau_{fc} \gtrsim 5$ s) can exhibit extended periods of nonlinear decay where the skin time is continuously changing as nearby superconducting tapes transition from saturated to nonsaturated states. In these cases, such as the spiral-wound FC discussed in Sec. VI.D, the critical current may in fact be a function of the driving current waveform, which makes it difficult to even define a single critical current value for the FC. In most cases of interest, however, the HTS-FCs exhibit a behavior similar to that shown in Fig. 11. In particular, t_{cr} appears to

be primarily a function of the shape of the driving current waveform $I_{dr}(t)$ (as opposed to its amplitude). Since the same driving current waveform is used in all of the HTS-FC tests conducted here, the critical time is consistently observed to be $t_{cr} \simeq 120$ ms. Thus, we are able to unambiguously define our measurement of I_{cr} to be the value of the log-linear fit to $I_{fc}(t)$ at $t = t_{cr} = 120$ ms.

The accuracy of the above definition for the experimentally measured critical current was verified by examining HTS-FCs that contain only a single turn of HTS tape. In this configuration, the critical current of the HTS-FC should very nearly be the factory-quoted I_{cr} value. Both available types of HTS tape ($I_{tape} = 160$ A and $I_{tape} = 64.2$ A) were tested in this manner, and in each case the experimentally measured I_{cr} value fell within 5% of the factory-quoted value.

VI. HTS-FC RESULTS

The primary goal of the prototype HTS-FC experiments that are presented here is to establish an understanding of the physical and technical considerations that govern the performance of the HTS-FC rings; in doing so, we can be confident that the desired performance parameters for the PFRC-2 HTS-FC rings (see Table I) can consistently be achieved. This requires a detailed understanding of how variables such as the winding configuration of the HTS tapes and the background operating temperature of the ring affect its overall performance. These concerns are addressed in this section through a series of controlled experiments with various HTS-FC rings.

VI.A. HTS Tape Number and Winding Configuration

During the initial testing of prototype HTS-FCs, it became clear that (a) the HTS tapes readily increase the skin time of the FC ring into the $\tau_{fc} > 0.1$ s range and (b) the actual HTS-FC skin time is strongly dependent on the winding configuration of the HTS tapes. Recall from Sec. IV that we are considering three different tape winding configurations (aligned gap, staggered gap, and spiral). In both the aligned and staggered configurations, each of the N turns of tape is broken at one location such that there are also N gaps. With the aligned configuration, the N gaps are all "aligned" at one azimuthal location such that the turns are in parallel. With the staggered configuration, on the other hand, the N gaps are distributed evenly (i.e., "staggered") around the FC ring. Finally, the spiral configuration simply contains one N-turn, series-connected "spiral" winding.

Sample $I_{fc}(t)$ waveforms from one aligned and one staggered HTS-FC, each with $N = 5$ turns of HTS tape, are shown in Fig. 12. In both cases, the driving current is small such that $I_{fc} < I_{cr}$ throughout. Also included for comparison are waveforms from room-temperature and
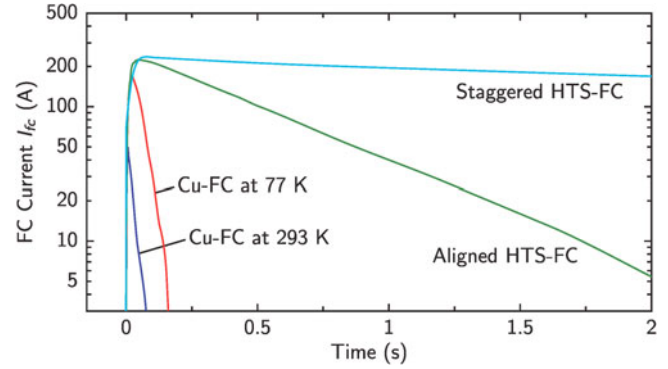

Fig. 12. Comparison of measured FC currents for various FC rings. Both of the HTS-FCs contain 5 turns of HTS tape. The skin time of a given FC can clearly be extended with HTS materials. It is also clear that τ_{fc} varies widely depending on the winding configuration of the HTS tapes (in this case, aligned or staggered).

LN$_2$-temperature OFHC copper FCs. The copper FCs have $\tau_{fc} \simeq 3.2$ ms and $\tau_{fc} \simeq 28.0$ ms, respectively. The HTS-FCs, on the other hand, have $\tau_{fc} \sim 500$ ms (aligned) and $\tau_{fc} \sim 10$ s (staggered). It is clear, then, that (a) the two HTS-FC skin times are much longer than those of the Cu-FCs and (b) the two HTS-FC skin times are substantially different from each other. Data from a spiral-wound FC is not shown here. These FCs exhibit an even longer skin time ($\tau_{fc} \gtrsim 100$ s) and will be discussed separately in Sec. VI.D.

It is clear from Fig. 12 that a deeper understanding of the role of the winding configuration is required. During these experiments, we also discovered that the performance of a given winding configuration (both τ_{fc} and I_{cr}) is sensitive to the number of HTS tapes embedded in the ring. Because the PFRC-2 HTS-FC rings will require many embedded HTS tapes ($N = 24$ to 26) in order to meet the $I_{cr} \simeq 2.5$ kA operational constraint, it is also imperative to understand how the performance of each winding configuration scales with HTS tape number. To this end, a detailed study of the tape number scaling of both the aligned and staggered configurations was performed.

For the tape number scaling study, HTS-FC rings were constructed in both the aligned and staggered configurations for various numbers of embedded HTS tapes N. Because of the limited amount of available HTS tape for these prototyping experiments, the study consists primarily of HTS-FCs in the low-N range ($N = 1$ to 5). Though this range is well below the 24 to 26 tapes that are required for the PFRC-2 HTS-FCs, this tape number scaling study provides valuable information as to the expected behavior at higher N. All of the HTS-FCs in this study were constructed using HTS tapes with $I_{tape} \simeq 64.2$ A.

The performance data (τ_{fc} and I_{cr}) gathered from the tape number scan are displayed in Fig. 13. Both the
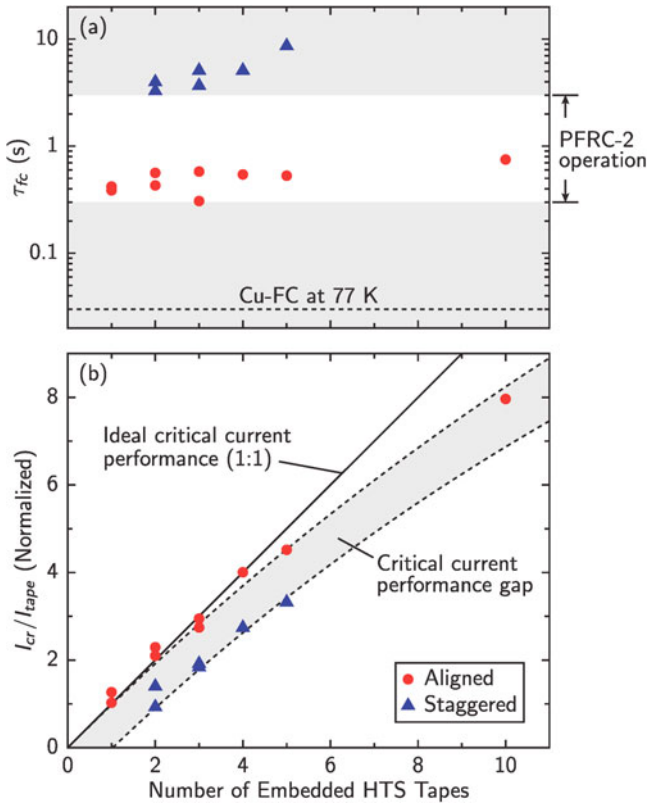
Fig. 13. Study of the scaling of the HTS-FC (a) skin time τ_{fc} and (b) critical current I_{cr} as the number of embedded HTS tapes is increased. Both the aligned and staggered tape alignment configurations are included.

Fig. 14. Data from a series of 2-tape HTS-FCs with different angles, θ, between the gaps in the two HTS-FC tapes. These data illustrate the transition between the behavior of an aligned HTS-FC and a staggered HTS-FC.

aligned and staggered configurations show similar behavior, with τ_{fc} nearly independent of N and with I_{cr} increasing with N. The aligned-configuration skin time is consistently in the 300 ms $< \tau_{fc} <$ 800 ms range, while the staggered-configuration skin time is longer (2 s $< \tau_{fc} <$ 10 s). The longer skin time for the staggered configuration comes with a clear penalty in I_{cr}, however, as the aligned configuration consistently outperforms the staggered configuration. The possible cause of this critical current performance gap will be discussed in Sec. VII. From this tape number scaling study, it is clear that the aligned configuration best fulfills the operational requirements of the PFRC-2 device. It has a consistent skin time in the desired operating regime and offers better critical current performance than the staggered configuration.

VI.B. HTS Tape Gap Angle Study

If the aligned configuration is to be used for the PFRC-2 HTS-FCs, it is important to understand how sensitive the HTS-FC performance is to the quality of the alignment at the single-gap location of the aligned
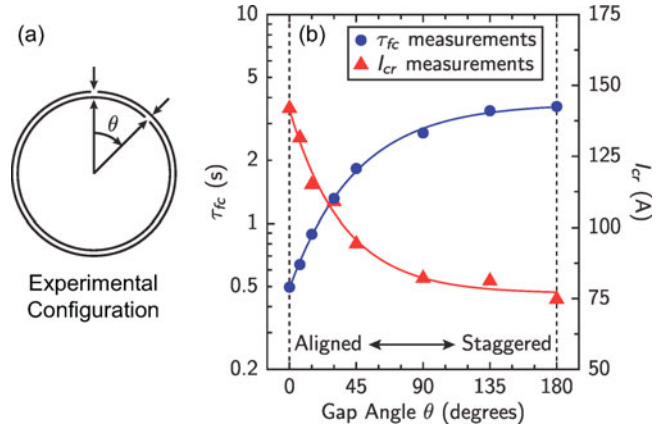
configuration. To study this in detail, a scan of 2-tape HTS-FCs was conducted where the angle between the gaps in the two HTS tapes, θ, was varied from $\theta = 0°$ to $\theta = 180°$. These limits correspond to a 2-tape aligned HTS-FC and a 2-tape staggered HTS-FC, respectively. A total of eight HTS-FCs were constructed for this scan, and their performance characteristics are shown in Fig. 14.

The primary conclusion is that the bulk of the transition from aligned behavior to staggered behavior occurs in the range $0° < \theta < 90°$. This indicates that the performance characteristics of the HTS-FC are determined by the overlap between adjacent tapes on the scale of a few centimeters (as opposed to a few millimeters). It is reassuring that the aligned configuration behavior is not lost with just a few degrees of misalignment. In practice, alignment to within this tolerance is easily achieved. The fact that the critical current performance of a 2-turn staggered HTS-FC is $I_{cr} \simeq I_{tape}$ hints that the current in the HTS-FC is being carried by just a single tape in the regions near the two staggered gaps. This assertion contributes to our understanding of the behaviors of the aligned and the staggered configurations (see Sec. VII).

VI.C. Temperature Dependence of FC Parameters

Because the electrical properties of the BSCCO superconductor used here varies with operating temperature, it also important to understand how the HTS-FC performance is affected by small changes in the operating temperature. This information gives an allowable operating temperature range and provides insight into the physics that determine HTS-FC behavior. Tests of prototype FCs are most easily carried out at the boiling point of LN$_2$ (77.3 K), but the FCs in the PFRC-2 will run at a

temperature that will be somewhat higher than that—about 1 to 10 K higher, depending on the performance of the cooling system and the heat loads in the device. The temperature-dependent HTS-FC experiments discussed here were conducted with temperature measurements from a LakeShore Model 218 silicon diode temperature monitor system, which is accurate to 0.01 K.

The skin time dependence of an aligned-gap HTS-FC with 10 turns of HTS tape ($I_{tape} \simeq 64.2$ A) is shown in Fig. 15a for seven different values of driving current I_{dr}. The skin time does not depend significantly on current but does decrease approximately linearly with increasing temperature. The endpoints of the temperature range studied are set by the boiling point of nitrogen and the critical temperature of BSCCO. All of these skin-time measurements were made at points in time when the induced current was less than I_{cr}. Note that the scatter in the τ_{fc} measurements increases at higher temperatures where the low induced currents make the measurements less accurate.
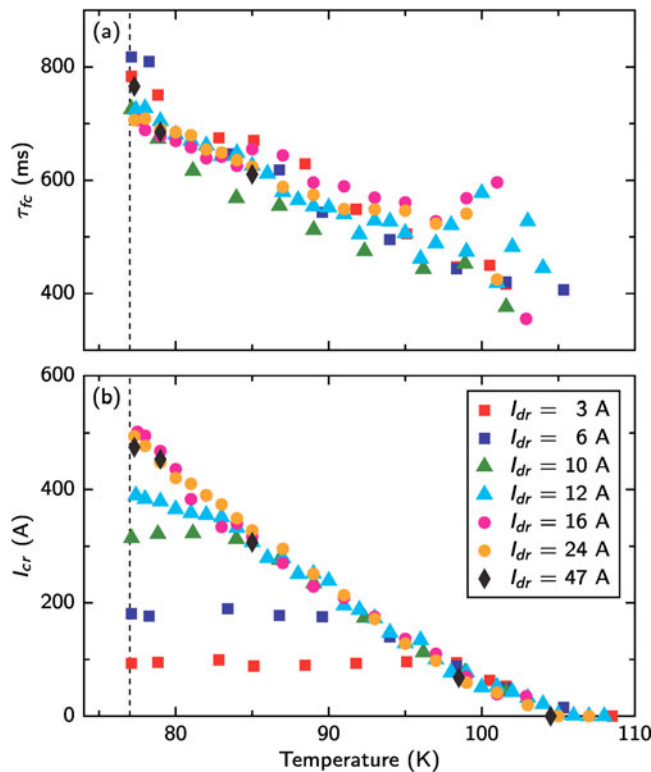

Fig. 15. (a) Skin time as a function of temperature for a 10-tape aligned HTS-FC ($I_{tape} = 64.2$ A) at several different values of driving current I_{dr}. Each data series corresponds to a temperature scan over one driving current. Note the suppressed zero on the y-axis. (b) Critical current as a function of temperature for the same HTS-FC. At higher driving currents, the HTS-FC is driven to saturation at all temperatures, so the maximum current values achieved at each temperature define the critical current curve $I_{cr}(T)$.

The relationship between skin time and temperature shown in Fig. 15a is described by the approximate formula:

$$\tau_{fc} \text{ (ms)} = -10.7T \text{ (K)} + 1540 \ . \qquad (16)$$

This corresponds to a decrease of 25% in skin time as temperature increases by 20 K. With the inductance assumed constant, this corresponds to an ~30% increase in the resistance of the of FC. This is similar to the increase in resistivity of copper over this temperature range, confirming the result of the ANSYS model (see Sec. VII) that most of the current flow across the gap is carried in the nearby copper instead of the solder in the gap. In fact, locally removing the solder from the gap in this experiment did not lower the skin time appreciably.

The critical current of an HTS-FC is also observed to decrease with increasing temperature and is directly related to changes in the critical current of the embedded HTS material. Above the BSCCO critical temperature, $I_{cr} = 0$ A. To analyze the critical current of the HTS-FC, the maximum current that could be induced by a particular driving current was graphed against the temperature of the FC. The results for the same 10-turn HTS-FC are shown in Fig. 15b. Because the HTS-FC is driven to saturation at higher driving currents, the curve produced by the maximum I_{cr} value at each temperature is the critical current dependence $I_{cr}(T)$ of the HTS-FC. At 77.3 K, $I_{cr} \simeq 500$ A, which is ~80% of the 10-tape ideal critical current capacity. The decrease in efficiency, where additional turns of tape contribute less than their own critical current value to the total I_{cr} of the FC, was seen in all of our earlier experiments (see Fig. 13b). We estimate that the cause of this loss of efficiency is a magnetic field effect due to the proximity of the tapes. Further experimentation and modeling are needed to fully understand this phenomenon.

Cooling of the HTS-FCs in the PFRC-2 chamber will be done by flowing LN_2 to the FCs through $\frac{1}{4}$-in. copper tubing soldered into a second trench in the FC, concentric with the HTS tapes. Tests of this method have shown that gravity-fed LN_2 can cool the FC to 79 K which, in conjunction with the temperature results in Fig. 15, ensures that little performance will be lost to thermal effects in the experiment.

VI.D. Spiral-Wound FCs

Spiral-wound HTS-FCs showed more complicated behavior than the copper FCs or the aligned or staggered HTS-FCs. Long and time-varying skin times were observed. The very long skin times that characterize spiral HTS-FCs make measurement of their properties more difficult. We made technical adjustments to ensure the accuracy of these measurements. Figure 16a shows the time dependence of the current induced in a 10-turn spiral HTS-FC at 77.3 K. The skin time, which is the inverse of the slope of the measured $I_{fc}(t)$ waveform, is seen to increase progressively for >10 s after the initial pulse.
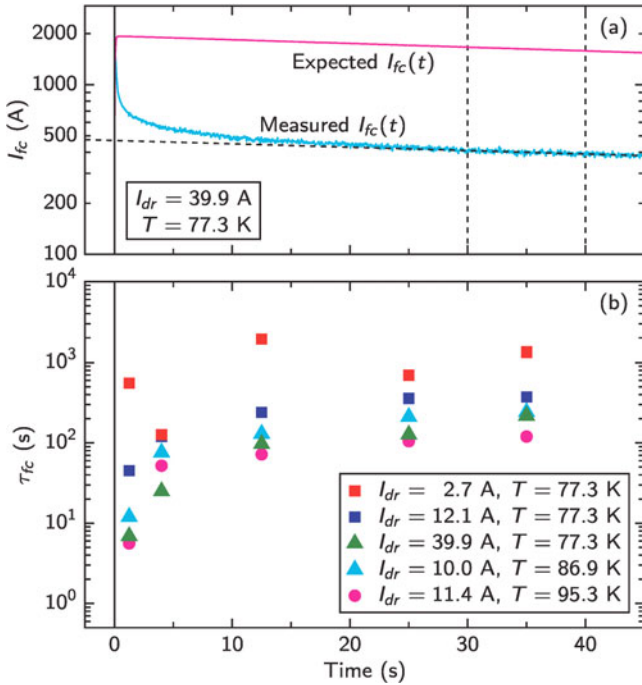
Fig. 16. (a) Current evolution for 10-turn spiral-wound HTS-FC at large driving current. (b) Skin times for different driving currents and temperatures measured at different times for the same spiral-wound HTS-FC. The time is the median time of the period over which the skin time measurement was made.

This is in contrast to the aligned-gap HTS-FC, which shows single-exponential behavior after $\sim$120 ms. The magnitude and duration of the effect also depend on current, with larger driving currents producing lower percentages of current retained at later times. A speculated reason is that, at high driving currents, the induced current quickly exceeds I_{cr} in the individual inner turns and must then redistribute itself to include turns farther out, hence increasing its inductance.

Figure 16b plots the changing τ_{fc} values against time for several trials with the same 10-turn spiral-wound FC. Note that, though the skin time in each trial approaches an asymptotic value after $\sim$25 s, both the driving current and the operating temperature strongly affect this asymptotic value. The longest skin times are achieved at the lowest driving currents and temperatures, while both higher driving currents and higher temperatures are observed to degrade spiral-wound FC performance.

VII. DISCUSSION

From the results presented in Sec. VI, it is clear that the mechanisms behind the behaviors of the various HTS-FC rings (both τ_{fc} and I_{cr}) are complex. In contrast,

the measured τ_{fc} of room-temperature and LN$_2$-cooled OFHC copper FC rings agrees very well with simple estimates. We will now discuss several mechanisms that could be responsible for the observed HTS-FC behaviors. In order to achieve the large disparity in $\tau_{fc} \equiv L_{fc}/R_{fc}$ that is observed between the aligned and staggered HTS-FCs, a significant change must occur in either the FC resistance R_{fc} or its inductance L_{fc}. It is likely that both of these parameters change among the different configurations, but it is the relative role of these two parameters that is the subject of some debate.

The resistance is affected by the details of the current path near the gaps in the HTS tapes, while the inductance is affected by global differences in the current path (i.e., traveling around a spiral). For thin circular coils of square cross section, Grover[13] presents the approximation of the inductance:

$$L = 0.001 a N^2 P'_o \ \mu\text{H} \ , \qquad (17)$$

where a (cm) is the coil average radius, N is the number of turns, and P'_o is a calculated/tabulated factor that depends on the ratio of the radial dimension (the breadth) of the cross section to a. Thus, L may be readily increased by two geometric changes:

1. reducing the breadth of the current-carrying element, which increases P'_o

2. increasing N.

The first effect occurs for times longer than the skin time of the copper, which is $\sim$28 ms for Cu at 77.3 K. The second effect only operates if the HTS is in a spiral-wound configuration. We will now discuss the implications of these considerations for each winding configuration.

The Aligned-Gap Winding Configuration

In the aligned-gap HTS-FCs, the current path is rather simple to envision. Because there is a single gap where all of the HTS tapes are broken, the current must cross some section of solder or copper in this region. Away from the gap region, on the other hand, the current is carried in the superconducting tapes only. Because the bulk of the induced azimuthal electric field exists in the gap region, equal currents will be driven in each of the HTS tapes. Thus, the multiple turns essentially behave as a single-turn narrow ring defined by the thickness of the HTS tapes and with a critical current $I_{cr} \sim NI_{tape}$. The thinness of the HTS tapes compared to the radial breadth of the FC increases the inductance about a factor of 1.5 to 2 compared to the solid Cu-FC. This factor depends weakly on the number of turns, in part because the tapes are of equal height.

The details of the gap region were modeled using a time-independent ANSYS simulation. For currents below the critical value, the resistance is determined by the LN$_2$-cooled solder in the gap of nominal width of 0.1 cm,

breadth of 0.2 cm, and depth of 0.5 cm and by the nearby copper. We have measured the resistivity of Sn/Pb eutectic solder and found $_{SnPb}\rho_{295K} \simeq 150$ nΩ·m and $_{SnPb}\rho_{77.3K} \simeq 10$ nΩ·m. Using these parameters as inputs for the simulations with 4 turns of soldered HTS tape, we

generated a plot of the voltage developed throughout the FC with 1 A of current flowing in the tapes (see Fig. 17). Near the gap, ~20% of the current flows through the solder and 80% through the nearby, lower-resistance copper. Based on these calculated resistances, we find the
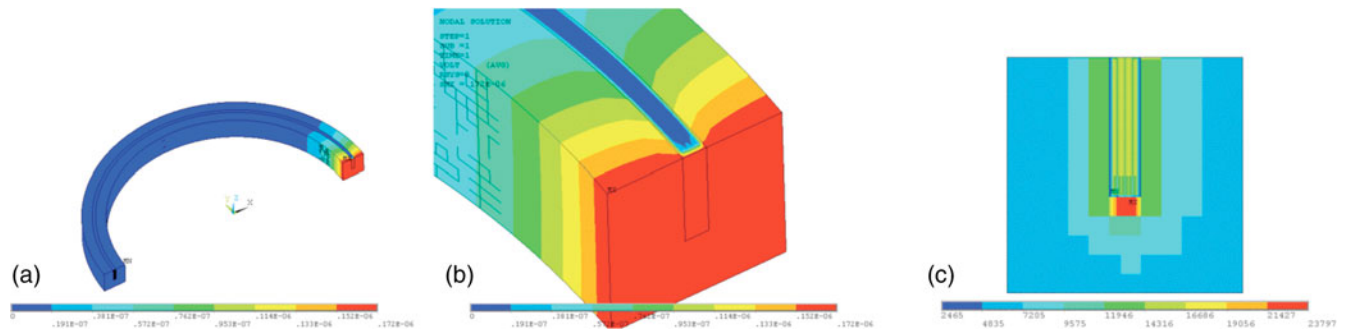

Fig. 17. (a) Voltage distribution in an FC with 4 HTS tapes having aligned gaps and carrying a total current of 1 A. The tapes are embedded in Sn/Pb solder, which also fills the 1-mm-wide, 0.5-cm-tall gap. (b) Close-up of region near the gap. (c) Current density normal to the gap's midplane. The high current density just below the HTS trench is caused by current that has leaked out the HTS tape lower edge and into the Cu. It accounts for ~3% of the total current.
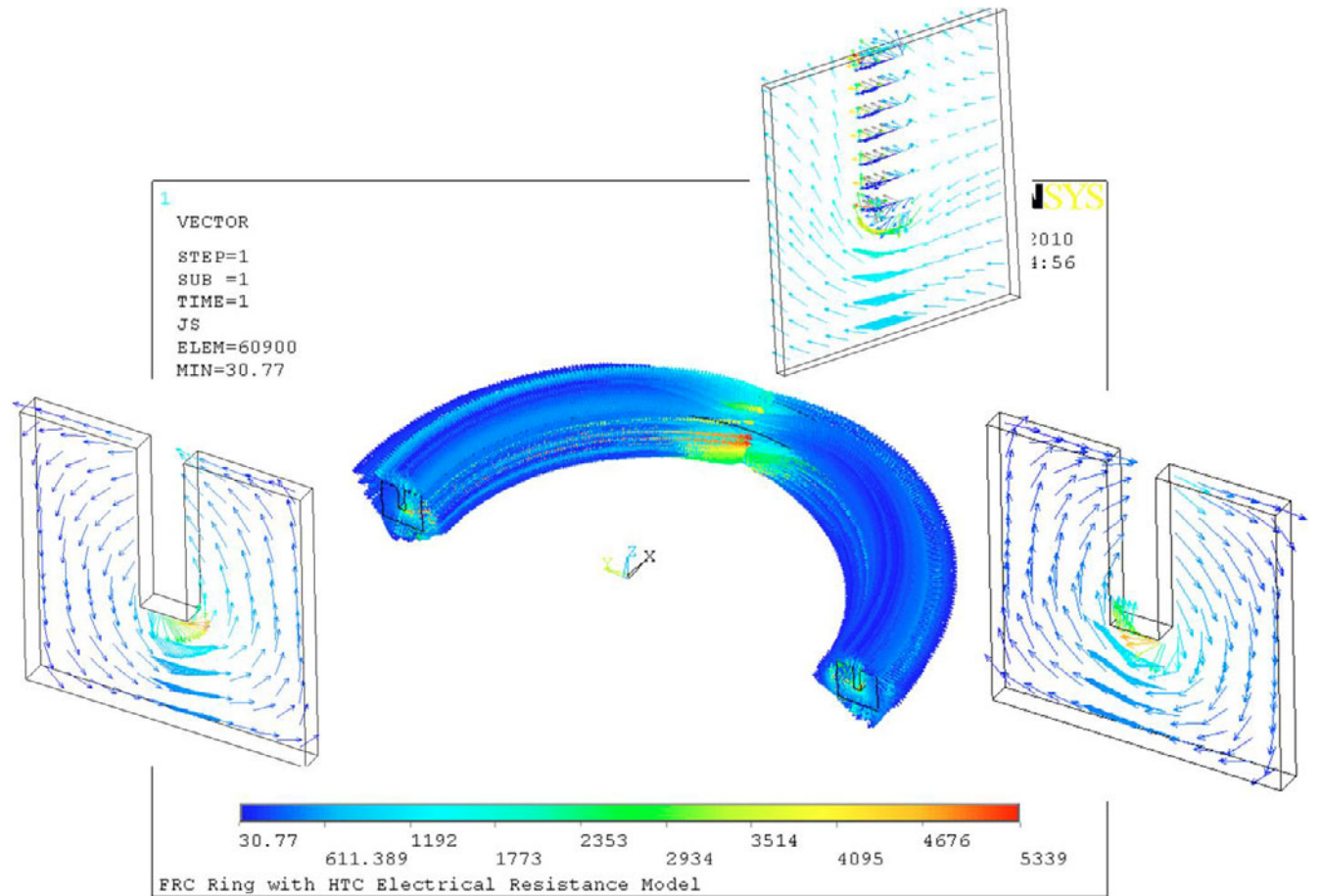

Fig. 18. An ANSYS model of current distribution in spiral FC. The ends of the tape are at the midpoint of the semicircle presented.

skin time to be ~ 1 s, which is 60% longer than the measured value. As seen in Fig. 17, the current near the gap does not flow only in the azimuthal direction. There is a slight outward radial bulge and a smaller axial displacement. Whether these magnetic field asymmetries cause a detrimental perturbation to the FRC plasma and perhaps opening of field lines has yet to be determined.

The Staggered-Gap Winding Configuration

The transition from an aligned HTS-FC to a staggered HTS-FC was studied in detail with the gap angle scan presented in Sec. VI.B. As discussed, the aligned case behaves as if the two tapes are a single turn of superconductor with twice the critical current capacity of a single HTS tape. In the staggered case, on the other hand, the critical current capacity is much closer to that of a single HTS tape, and the skin time increases significantly. An explanation that is consistent with both the drop in I_{cr} and the rise in τ_{fc} is that when a gap in one of the tapes is spanned continuously by an adjacent tape (as in the staggered-gap case), the current from the tape that is broken at the gap transfers to the adjacent tape that spans the gap. This current path that weaves from HTS tape to HTS tape evidently has a much lower resistance than the current path across the single gap in the aligned case.

Support for this hypothesis comes from experiments in which we placed short pieces of HTS tape alongside aligned gaps and found notable increases in the skin time. As a corollary, when the current transfers completely from one tape to another in each of the gap regions, the critical current capacity of the 2-turn ring is reduced to that of a single tape because one tape is carrying all of the current. This theory of current transfer between adjacent HTS tapes can be extended to explain the first-order behavior that was observed in the tape number scaling study (see Sec. VI.A). The staggered-configuration HTS-FCs have a consistently longer skin time and lower critical current (by about one tape) than their aligned counterparts such that $I_{cr} \sim (N-1)I_{tape}$. It is possible that the inductance of the staggered configuration is also slightly higher due to the narrowed current path, but this effect would be smaller than the reduced resistance.

The Spiral-Wound Configuration

Finally, the most complex behavior comes from the spiral-wound HTS-FC. It is possible that a change in self-inductance is responsible for most of the increase in the skin time if the current flows in the spiral path rather than in parallel as it does through the aligned-gap FC. Alternatively, if the current flows from the edges of the HTS tapes to nearby turns, a lower resistance will result. The total self-inductance for an FC modeled as an N-turn spiral differs from the self-inductance of an FC made of a single loop by a factor of N^2 [see Eq. (17)]. Since $N=10$ for the FC under consideration and the skin time

for the spiral FC is ~ 100 to 200 times greater than the skin time for the aligned-gap FC, this is a reasonable source of the change. The proposed current path would then run from end to end of the spiral inside the single piece of HTS tape before running azimuthally around all the tapes to complete the circuit.

This assertion is supported by a time-independent ANSYS model, which shows that the current moves helically outside of the superconductor predominantly near the tape ends (see Fig. 18). Alternatively and in the time-varying phase of the problem, the current may still flow in parallel, jumping between only the tape edges at many separate places. The transverse jump sideways between tapes may be much less resistive than the forward jump across the gap in the aligned case. Movement of the jump regions may also contribute to the time dependence of skin time discussed earlier. A better understanding of this problem will require significant future work experimentally and computationally, particularly with time-dependent codes that include precise properties of the HTS tape, including magnetic-field-dependent critical current.

VIII. SUMMARY

In this paper we have motivated and described the passive, internal array of eight HTS-FC rings that will be implemented on the PFRC-2 device. A series of prototyping experiments was used to study three different tape-winding configurations (aligned gap, staggered gap, and spiral). A significant understanding of the mechanisms that govern each configuration's behavior was obtained, though further opportunities for experimentation and simulation certainly exist. Most importantly, we determined that the skin time and critical current performance requirements of the PFRC-2 device are best met by aligned-gap HTS-FCs with 24 to 26 turns of HTS tape. We found that these aligned-gap HTS-FCs can be manufactured consistently and that small variations in operating temperature will not significantly degrade their performance. The eight HTS-FC rings for the PFRC-2 device are presently being constructed. Preliminary results indicate that they have 0.9 s $\leq \tau_{fc} \leq 1.1$ s and 2.8 kA $\leq I_{cr} \leq 3.1$ kA.

REFERENCES

1. H. MOMOTA et al., "Conceptual Design of the D-^{3}He Reactor Artemis," *Fusion Technol.*, **21**, 2307 (1992).

2. H. A. BLEVIN and P. C. THONEMANN, "Plasma Confinement Using an Alternating Magnetic Field," *Nucl. Fusion Suppl., Part I*, 55 (1962).

3. A. H. GLASSER and S. A. COHEN, "Ion and Electron Acceleration in the Field-Reversed Configuration with Odd-Parity Rotating Magnetic Field," *Phys. Plasmas*, **9**, 2093 (2002).

4. S. A. COHEN, "Dynamical Stabilization of the Internal Tilt Mode by Rotating Magnetic Fields," *Bull. Am. Phys. Soc.*, **44**, 596 (1999).

5. S. A. COHEN et al., "Formation of Collisionless High-Beta Plasmas by Odd-Parity Rotating Magnetic Fields," *Phys. Rev. Lett.*, **98**, 072508 (2007).

6. C. BRUNKHORST, B. BERLINGER, N. FERRARO, and S. A. COHEN, "The Princeton FRC Rotating-Magnetic-Field-Experiment RF System," *Proc. 22nd IEEE/NPSS Symp. Fusion Engineering*, Albuquerque, New Mexico, June 17–21, 2007, p. P2, Symposium on Fusion Engineering.

7. S. A. COHEN and R. D. MILROY, "Maintaining the Closed Magnetic-Field-Line Topology of a Field-Reversed Configuration with the Addition of Static Transverse Magnetic Fields," *Phys. Plasmas*, **7**, 2539 (2000).

8. D. C. BARNES, "Stability of Long Field-Reversed Configurations," *Phys. Plasmas*, **9**, 560 (2002).

9. D. R. WELCH, S. A. COHEN, T. GENONI, and A. GLASSER, "Formation of Field-Reversed-Configuration Plasma with Punctuated-Betatron-Orbit Electrons," *Phys. Rev. Lett.*, **105**, 015002 (2010).

10. R. D. MILROY, "A Numerical Study of Rotating Magnetic Fields as a Current Drive for Field Reversed Configurations," *Phys. Plasmas*, **6**, 2771 (1999).

11. D. W. WEISSENBURGER, "SPARK Version 1.1 User Manual," PPPL-2494, Princeton Plasma Physics Laboratory (1988).

12. P. C. STANGEBY, *The Plasma Boundary of Magnetic Fusion Devices*, Institute of Physics Pub., Philadelphia, Pennsylvania (2000).

13. F. W. GROVER, *Inductance Calculations*, Dover Phoenix Editions, New York (1946).